Computational Mechanics
https://doi.org/10.1007/s00466-024-02572-3

ORIGINAL PAPER

A strategy for scaling the hardening behavior in finite element modelling of geometrically exact beams

T. Gärtner[1,2] · S. J. van den Boom[2] · J. Weerheijm[1] · L. J. Sluys[1]

Received: 16 July 2024 / Accepted: 11 October 2024

Abstract
A yield function in the stress resultant space of geometrically exact beams based on the elastoplastic cross-sectional warping problem has been proposed by Herrnböck et al. (Comput Mech, 67(3):723–742, 2021). This plasticity framework has been extended with a hardening tensor to model the kinematic hardening effects in Herrnböck et al. (Comput Mech, 71(1):1–24, 2022). While this framework provides scaling for the yield surface in ideal plasticity, scaling in hardening plasticity has not yet been explored. This paper focuses on the numeric modelling of hardening beams and beam assemblies at different geometric scales. Discretization effects from the introduction of plasticity into the geometrically exact beam model are demonstrated. Furthermore, the effects of scaling are explored, and a method to mitigate undesirable effects in order to achieve a size-agnostic formulation is proposed. Consistent geometric scaling is demonstrated for two alternative scaling approaches of the yield function.

Keywords Geometrically exact beams · Hardening plasticity · Geometric scaling · Elastoplasticity

1 Introduction

Beams undergo large, plastic deformations in various applications, such as the weaving of chain-link fences, the production of paper clips, or the crushing of architected lattice materials. The latter are man-made structures in demand for a wide range of applications, from sports equipment to protective systems in a military context [1–3]. These lattice materials, can be seen as a collection of beams, and are represented accordingly in a finite element (FE) context. In the given applications, metal lattices undergo large deformations that may include material nonlinearities. In order to design such materials, a proper representation of the beams undergoing large deformations with the corresponding inelastic material behavior is required. The representation of beams undergoing large deformations with elastic material behavior following the Simo-Reissner (after [4, 5]) beam theory is well established under various names such as nonlinear Timoshenko beams or special Cosserat rods (see also [6, 7]).

Irreversible deformation of the beam structures, i.e., plasticity, is not considered in these formulations. When including plasticity into the beam models, one has two options: The plastic deformation can be concentrated at distinct cross-sections throughout the beam, or it can be distributed over the entire beam. The first approach corresponds to so-called *plastic hinges*, represented by strong discontinuities along the beam and thus introduced as such into the FE model [8, 9]. The second approach is to introduce plasticity into the description of the beam-type strain measures of the beam itself. [10] present a thermoelastoplastic formulation for such an approach, with an FE implementation described in [11]. A similar approach is taken by [12], where a formulation for elasto-visco-plastic beams is presented in an isogeometric framework. The introduction of plasticity into the strain and curvature measures of the beam is closest to traditional continuum plasticity and straightforward to be implemented in an existing framework, as no changes in the geometric representation are required. One problem not solved in these approaches is, however, the determination of a yield criterion for the formulation at hand. This issue could be relegated back to the material scale by introducing a *sub*integration across the cross-section in each integration point of the beam

✉ T. Gärtner
t.gartner@tudelft.nl

1 Faculty of Civil Engineering and Geosciences, Delft University of Technology, PO Box 5048, 2600 GA Delft, The Netherlands

2 Netherlands Institute for Applied Scientific Research (TNO), PO Box 480, 2501 CL The Hague, The Netherlands

Published online: 15 November 2024

element, as presented in [13]. This approach is also used in most commercial FE codes.

For the purpose of this investigation, however, a yield surface in the six-dimensional stress-resultant space is chosen, in order to ensure fast computation. Early approaches to this are limited to simple deformations and do not include any hardening behavior of the material [14, 15]. More recently, [16] formulate an approach to systematically determine the yield surface using the formulation of [10, 11] for a given cross-section and material model, based on simulations of the cross-section on the material scale. The procedure is demonstrated with a J2-plasticity model for a generic steel in beams with circular and square cross-sections. The authors also demonstrate the geometric scaling behavior of the resulting yield surface. This can be motivated based on the fact, that the beam-type stresses are essentially cross-sectional forces and moments. They extend their approach to kinematic hardening in [17] for the circular cross-section without considering geometric scaling. The extension demonstrates a good agreement with a FE^2 approach utilizing the identical plasticity model in their test cases. The discrepancies observed can be attributed to the fact that, in the stress-resultant approach, the entire cross-section plastifies simultaneously, whereas in reality a more gradual plastification process occurs [17]. It is shown how the kinematic hardening tensor is a full matrix and that it relates to microscale isotropic hardening, that is assumed for the underlying material behavior. The geometric scaling of hardening plasticity in beam formulations has not been investigated so far in literature. However, it is of paramount importance for the targeted design of lattice materials structures exposed to severe straining.

In this work, we investigate the geometric scaling behavior of the kinematic hardening formulation of [17]. We suggest an adequate scaling approach to be used in the design process of lattice structures representing metal metamaterials undergoing large inelastic deformations. In Sect. 2 the theoretical background for our investigations is laid out, followed by a mesh convergence study in Sect. 3. The extent of the geometric scaling in the existing formulation, not considering the hardening tensor, is demonstrated in Sect. 4 using a simple bending cantilever together with its limitations, followed by our proposal to mitigate this effect. We demonstrate in Sect. 5, how to apply the proposed strategy to different yield functions and present the results in a three-dimensional setting.

2 Theoretical background

Shear-flexible beams with a rigid cross-section undergoing large deformations can be described as nonlinear Timoshenko beams, known as well as Simo-Reissner beams [4, 5] or special Cosserat rods [6]. The theoretical description of these beams is presented first in Sect. 2.1 in an elastic context. The introduction of plasticity into this framework will be subsequently explained. Lastly, the yield surfaces and their scaling are shown and the implicit geometric scaling of the hardening tensor is introduced. In Sect. 2.2 the implementation into an FE-framework with the introduction of plasticity and an explicit return mapping scheme in the form of a convex cutting-plane algorithm using the JIVE-framework [18] are presented.

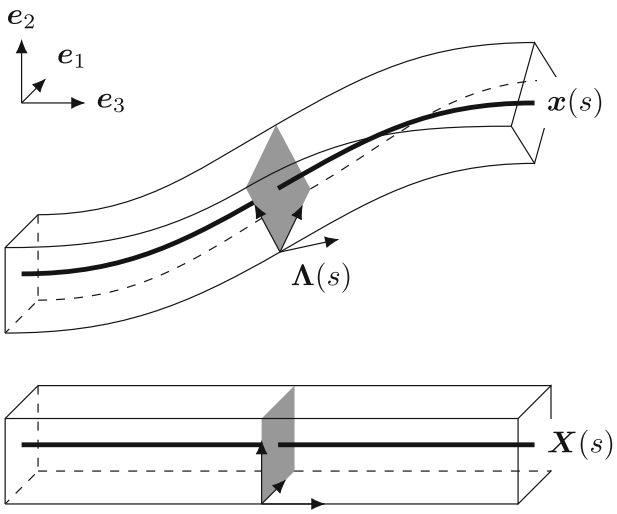

Fig. 1 Schematic of the beam in its undeformed (bottom) and deformed (top) configuration

2.1 Beam description

The following explanations for describing the beam element are based on [6, 7]. The beam is described by its centerline $\boldsymbol{x}(s)$ and the three orthonormal directors $\boldsymbol{d}_1(s), \boldsymbol{d}_2(s), \boldsymbol{d}_3(s)$ attached to it. These three directors serve as the column vectors of the rotation matrix $\boldsymbol{\Lambda}$ between the global frame of reference and the local coordinate frame of the cross-section at arc-length s (see Fig. 1):

$$\boldsymbol{\Lambda}(s) = \boldsymbol{d}_i(s) \otimes \boldsymbol{e}_i = \left[\boldsymbol{d}_1(s)\ \boldsymbol{d}_2(s)\ \boldsymbol{d}_3(s)\right]. \tag{1}$$

As this rotation represents the orientation of the rigid cross-section at a point along the center line $\boldsymbol{x}(s)$, it is later used to describe the curvature and torsion of the beam. For the description of extension and shearing of the beam, the current position of the centerline is expressed as the sum of the reference center line $\boldsymbol{X}$ and the deformation $\boldsymbol{u}$ according to

$$\boldsymbol{x}(s) = \boldsymbol{X}(s) + \boldsymbol{u}(s). \tag{2}$$

Summarizing, the entire deformation of the beam, as depicted in Fig. 1, is described by a mapping from the arc-

length coordinate to the current position of the center and orientation of the rigid beam cross-section.

$$s \mapsto (\boldsymbol{\Lambda}, \boldsymbol{x}) \quad \mathbb{R} \mapsto \mathrm{SO}(3) \times \mathbb{R}^3. \tag{3}$$

For the description of strains, it is useful to introduce the derivative with respect to s as $(\cdot)'$. The translational strains (shear and extension) $\boldsymbol{\gamma}(s)$ are expressed as

$$\boldsymbol{\gamma}(s) = \boldsymbol{x}'(s) - \boldsymbol{d}_3(s) \tag{4}$$

and the rotational strains (bending and torsion) $\boldsymbol{\kappa}$ are expressed as

$$\widetilde{\boldsymbol{\kappa}}(s) = \boldsymbol{\Lambda}'(s)\boldsymbol{\Lambda}^T(s), \tag{5}$$

with $\widetilde{(\cdot)}$ denoting a skew symmetric matrix with its associated axial vector. These strain components are summarized in the strain vector $\boldsymbol{\varepsilon} = \left[\boldsymbol{\gamma}\ \boldsymbol{\kappa}\right]^T$. For the calculation of the material response, these strains need to be expressed in the material frame, which can be done as:

$$\boldsymbol{\Gamma}(s) = \boldsymbol{\Lambda}^T(s)\left(\boldsymbol{x}'(s) - \boldsymbol{d}_3(s)\right), \tag{6}$$

$$\widetilde{\boldsymbol{\mathcal{K}}}(s) = \boldsymbol{\Lambda}^T(s)\boldsymbol{\Lambda}'(s), \tag{7}$$

where $\boldsymbol{\Gamma}$ represents the translational strains, $\boldsymbol{\mathcal{K}}$ the rotational strains, and they are summarized in $\boldsymbol{\mathcal{E}} = \left[\boldsymbol{\Gamma}\ \boldsymbol{\mathcal{K}}\right]^T$. The initial, elastic response can be described by relating the material strains to the material stress resultants $\boldsymbol{\Sigma}$, with $\boldsymbol{N}$ describing the forces and $\boldsymbol{M}$ the moments:

$$\boldsymbol{\Sigma}(s) = \begin{bmatrix}\boldsymbol{N}(s)\\ \boldsymbol{M}(s)\end{bmatrix} = \boldsymbol{C}\begin{bmatrix}\boldsymbol{\Gamma}(s)\\ \boldsymbol{\mathcal{K}}(s)\end{bmatrix} = \boldsymbol{C}\boldsymbol{\mathcal{E}}(s), \tag{8}$$

where the material stiffness matrix $\boldsymbol{C}$, in the context of point-symmetric cross-sections showing homogeneous, isotropic material distributions, is expressed using the engineering constants E as the Young's modulus, G as the shear modulus, A as the area of the cross-section, I_1, I_2 as the area moments of inertia in the directions of the directors $\boldsymbol{d}_1$, $\boldsymbol{d}_2$, J as the polar moment of inertia, and k as the shear correction coefficient:

$$\boldsymbol{C} = \begin{bmatrix} kGA & 0 & 0 & 0 & 0 & 0\\ 0 & kGA & 0 & 0 & 0 & 0\\ 0 & 0 & EA & 0 & 0 & 0\\ 0 & 0 & 0 & EI_1 & 0 & 0\\ 0 & 0 & 0 & 0 & EI_2 & 0\\ 0 & 0 & 0 & 0 & 0 & GJ \end{bmatrix}. \tag{9}$$

It should be mentioned here, that this material stiffness matrix *implicitly* scales with changes in the geometry, as the area and its second moments are defined using the geometry of the cross-section. This implicit scaling refers to the fact that the terms do not have a geometric scaling factor *explicitly* present in their analytical definition, but are naturally adapted based on the geometry. For instance, the area $A = \pi r^2$ is not defined by a scaling factor, but it is defined by the radius r, which is assumed to be scaled with the rest of the geometry. The stress resultants are also expressed in the inertial frame of reference, again using lower case symbols $\boldsymbol{\sigma} = \left[\boldsymbol{n}\ \boldsymbol{m}\right]^T$:

$$\boldsymbol{n}(s) = \boldsymbol{\Lambda}(s)\boldsymbol{N}(s), \tag{10}$$

$$\boldsymbol{m}(s) = \boldsymbol{\Lambda}(s)\boldsymbol{M}(s). \tag{11}$$

While the description thus far is purely elastic, beams undergoing large deformations are expected to exhibit inelastic behavior. This inelastic behavior must be captured in the numerical description as well. Here, we focus our attention on the description of kinematic hardening plasticity in the six-dimensional stress resultant space of a beam, following [10, 16, 17].

First, the strains are additively decomposed into elastic and plastic parts as in [10]:

$$\boldsymbol{\mathcal{E}} = \boldsymbol{\mathcal{E}}^e + \boldsymbol{\mathcal{E}}^p. \tag{12}$$

Using this decomposition, we can introduce the Helmholtz energy density Ψ from [10]:

$$\Psi = \frac{1}{2}\boldsymbol{\mathcal{E}}^{eT}\boldsymbol{C}\boldsymbol{\mathcal{E}}^e + \frac{1}{2}\boldsymbol{\mathcal{M}}^T\boldsymbol{H}\boldsymbol{\mathcal{M}}, \tag{13}$$

with the invertible, symmetric, constant 6×6 hardening tensor $\boldsymbol{H}$ and the internal hardening variables $\boldsymbol{\mathcal{M}} = \left[\mathcal{M}_1^\Gamma\ \mathcal{M}_2^\Gamma\ \mathcal{M}_3^\Gamma\ \mathcal{M}_1^\mathcal{K}\ \mathcal{M}_2^\mathcal{K}\ \mathcal{M}_3^\mathcal{K}\right]^T$. Furthermore, the yield function in the stress resultant space as proposed in [17] is introduced as

$$\begin{aligned}\Phi = &\left|\frac{N_1}{N_1^y - N_1^h}\right|^{\alpha_1^N} + \left|\frac{N_2}{N_2^y - N_2^h}\right|^{\alpha_2^N}\\ &+ \left|\frac{N_3}{N_3^y - N_3^h}\right|^{\alpha_3^N} + \left|\frac{M_1}{M_1^y - M_1^h}\right|^{\alpha_1^M}\\ &+ \left|\frac{M_2}{M_2^y - M_2^h}\right|^{\alpha_2^M} + \left|\frac{M_3}{M_3^y - M_3^h}\right|^{\alpha_3^M} - 1\\ &\leq 0.\end{aligned} \tag{14}$$

The hardening stresses $\boldsymbol{\Sigma}^h = \left[N^h\ \boldsymbol{M}^h\right]^T$ in this equation can be determined using the internal hardening variables $\boldsymbol{\mathcal{M}}$ and the hardening tensor $\boldsymbol{H}$ as shown in [10]:

$$\boldsymbol{\Sigma}^h = -\frac{\partial\Psi}{\partial\boldsymbol{\mathcal{M}}} = -\frac{1}{2}\frac{\partial(\boldsymbol{\mathcal{M}}^T\boldsymbol{H}\boldsymbol{\mathcal{M}})}{\partial\boldsymbol{\mathcal{M}}} = -\boldsymbol{H}\boldsymbol{\mathcal{M}}. \tag{15}$$

The associative flow rule introduced in [10] is expressed for the rate of the plastic strains $\boldsymbol{\mathcal{E}}^p$ and for the rate of the internal hardening variables $\boldsymbol{\mathcal{M}}$:

$$\dot{\boldsymbol{\mathcal{E}}}^p = \dot{\lambda}\frac{\partial \Phi}{\partial \boldsymbol{\Sigma}}, \quad \dot{\boldsymbol{\mathcal{M}}} = \dot{\lambda}\frac{\partial \Phi}{\partial \boldsymbol{\Sigma}^h}, \tag{16}$$

with the plastic multiplier $\dot{\lambda}$ from [11]

$$\dot{\lambda} = \frac{\frac{\partial \Phi}{\partial \boldsymbol{\Sigma}}\boldsymbol{C}\dot{\boldsymbol{\mathcal{E}}}}{\frac{\partial \Phi}{\partial \boldsymbol{\Sigma}}\boldsymbol{C}\frac{\partial \Phi}{\partial \boldsymbol{\Sigma}} + \frac{\partial \Phi}{\partial \boldsymbol{\Sigma}^h}\boldsymbol{H}\frac{\partial \Phi}{\partial \boldsymbol{\Sigma}^h}}, \tag{17}$$

and the Karush-Kuhn-Tucker conditions:

$$\dot{\lambda} \geq 0, \quad \Phi \leq 0, \quad \dot{\lambda}\Phi = 0. \tag{18}$$

2.2 FE formulation

For the FE discretization, this study follows the approach in [19] for the determination of the stiffness matrices and the resulting nodal forces. Linear Lagrangian shape functions are used to interpolate the position and position vectors, with reduced integration utilizing a single integration point per element to avoid shear-locking. The rotation matrices representing the orientation of the cross-sections are interpolated using spherical interpolation as demonstrated by [20].

For plasticity an explicit convex cutting-plane algorithm following [21] is implemented in the JIVE-framework. This leads to the loss of global quadratic convergence in an implicit, static solution scheme. However, it provides a fast and accurate solution in the context of an explicit scheme. In the following the explicit procedure is laid out following [21] using the notation used in this manuscript with an overview given in Algorithm 1.

Step 1 We initialize the local iteration variable $l = 0$, the linearized plastic flow $\Delta\lambda^{(0)} = 0$, the plastic strain $\boldsymbol{\mathcal{E}}_{n+1}^{p^{(0)}} = \boldsymbol{\mathcal{E}}_n^p$, and the hardening variables $\boldsymbol{\mathcal{M}}_{n+1}^{(0)} = \boldsymbol{\mathcal{M}}_n$, where the index n represents the converged solution for the last load step and $n+1$ the load step of the current global Newton–Raphson iteration.

Step 2 The stresses and hardening stresses are computed according to the constitutive relationships and subsequently the yield function at the current iteration $\Phi_{n+1}^{(l)}$ is evaluated using Eq. 14. If the yield function is smaller than a predefined tolerance $\Phi_{n+1}^{(l)} < \Phi_{\text{tol}}$, the iterative procedure has converged, and we can move forward with the global iterations, if not, we proceed with the next step.

Algorithm 1 Explicit return mapping iterations

Step 1: Initialize
$\boldsymbol{\mathcal{E}}_{n+1}^{p^{(0)}} = \boldsymbol{\mathcal{E}}_n^p, \quad \boldsymbol{\mathcal{M}}_{n+1}^{(0)} = \boldsymbol{\mathcal{M}}_n$
$\Delta\lambda^{(0)} = 0, \quad l = 0$

Step 2: Compute stresses and yield function
$\boldsymbol{\Sigma} = \boldsymbol{C}\left(\boldsymbol{\mathcal{E}}_{n+1} - \boldsymbol{\mathcal{E}}_{n+1}^{p^{(l)}}\right), \quad \boldsymbol{\Sigma}^h = -\boldsymbol{H}\boldsymbol{\mathcal{M}}_{n+1}^{(l)}$
Evaluate $\Phi_{n+1}^{(l)} = \Phi(\boldsymbol{\Sigma}, \boldsymbol{\Sigma}^h)$ using Eq. (14)

If $\Phi_{n+1}^{(l)} < \Phi_{\text{tol}}$
Finish procedure

Step 3: Compute plastic flow update
$\Delta^2\lambda = \frac{\Phi_{n+1}^{(l)}}{\partial_{\boldsymbol{\Sigma}}\Phi^{(l)}\boldsymbol{C}\partial_{\boldsymbol{\Sigma}}\Phi^{(l)} + \partial_{\boldsymbol{\Sigma}^h}\Phi^{(l)}\boldsymbol{H}\partial_{\boldsymbol{\Sigma}^h}\Phi^{(l)}}$

Step 4: Update plastic variables
$\Delta\lambda^{(l+1)} = \Delta\lambda^{(l)} + \Delta^2\lambda$
$\boldsymbol{\mathcal{E}}_{n+1}^{p^{(l+1)}} = \boldsymbol{\mathcal{E}}_{n+1}^{p^{(l)}} + \Delta^2\lambda\,\partial_{\boldsymbol{\Sigma}}\Phi^{(l)}$
$\boldsymbol{\mathcal{M}}_{n+1}^{(l+1)} = \boldsymbol{\mathcal{M}}_{n+1}^{(l)} + \Delta^2\lambda\,\partial_{\boldsymbol{\Sigma}^h}\Phi^{(l)}$

Increase local iteration variable $l = l + 1$
and go to **Step 2**

Step 3 The derivatives of the yield function at the current point are evaluated

$$\partial_{\boldsymbol{\Sigma}}\Phi^{(l)} = \frac{\partial \Phi}{\partial \boldsymbol{\Sigma}}(\boldsymbol{\Sigma}^{(l)}, \boldsymbol{\Sigma}^{h^{(l)}}),$$
$$\partial_{\boldsymbol{\Sigma}^h}\Phi^{(l)} = \frac{\partial \Phi}{\partial \boldsymbol{\Sigma}^h}(\boldsymbol{\Sigma}^{(l)}, \boldsymbol{\Sigma}^{h^{(l)}}).$$

Next, the increment $\Delta^2\lambda$ to the linearized plastic flow $\Delta\lambda^{(l)}$ is computed.

Step 4 Finally, we update the plastic flow, plastic strain, and internal hardening variables using the flow rules from Eq. 16. After incrementing the local iteration variable $l = l + 1$, one returns to **Step 2**.

The yield surface is in [16] derived for J2-plasticity and isotropic hardening with

$$\begin{aligned} N_1^y &= N_2^y = 700\ \text{N}, \\ N_3^y &= 1470\ \text{N}, \\ M_1^y &= M_2^y = 0.62\ \text{Nm}, \\ M_3^y &= 0.56\ \text{Nm}, \end{aligned} \tag{19}$$

and the exponents for the yield function Eq. 14 as

$$\begin{aligned} \alpha_1^N &= \alpha_2^N = 2.04, \\ \alpha_3^N &= 1.76, \\ \alpha_1^M &= \alpha_2^M = 2.09, \\ \alpha_3^M &= 1.73. \end{aligned} \tag{20}$$

For details regarding the used model, the reader is referred to the original contribution [16]. The authors also report an *implicit* scaling of the yield surface is with the area for the stress resultant force $\boldsymbol{N}^y$ components, by showing an excellent fit of the reported values with ϑ^2, where ϑ represents a geometric scaling factor. The stress resultant moments $\boldsymbol{M}^y$ are likewise *implicitly* scaled by the volume, as is demonstrated by the fit to ϑ^3. For hardening plasticity, the hardening tensor $\boldsymbol{H}$ was derived in [17], again for the identical plasticity model on the microscale:

$$\boldsymbol{H} = \begin{bmatrix} \boldsymbol{H}_{\varepsilon\varepsilon} & \boldsymbol{H}_{\varepsilon\kappa} \\ \boldsymbol{H}_{\kappa\varepsilon} & \boldsymbol{H}_{\kappa\kappa} \end{bmatrix}, \tag{21}$$

with submatrices:

$$\boldsymbol{H}_{\varepsilon\varepsilon} = \begin{bmatrix} 19014 & 17547 & 33121 \\ & 19014 & 33121 \\ \text{sym} & & 56864 \end{bmatrix} \text{N},$$

$$\boldsymbol{H}_{\varepsilon\kappa} = \begin{bmatrix} 16.069 & 16.743 & 15.552 \\ 16.743 & 16.069 & 15.556 \\ 24.578 & 24.578 & 26.757 \end{bmatrix} \text{Nm} = \boldsymbol{H}_{\kappa\varepsilon}^T,$$

$$\boldsymbol{H}_{\kappa\kappa} = \begin{bmatrix} 0.015015 & 0.015009 & 0.012715 \\ & 0.016015 & 0.012715 \\ \text{sym} & & 0.010434 \end{bmatrix} \text{Nm}^2.$$

In [17], the authors demonstrate the applicability of this approach with several examples of complex three-dimensional loading scenarios for beams. These examples also illustrate the limitations of this approach, which is that the entire cross-section plasticizes at once, as opposed to a gradual plastification when the cross-section is resolved at the microscale. This is particularly evident at the onset of plasticity in bending or torsion, where the fully resolved model shows a gradual transition from the elastic to the plastic regime. The stress resultant approach used here shows a sharp kink in the corresponding global load–displacement curves for the onset of plasticity over the entire cross-section. For further details and illustration of this process, the reader is referred to [17].

3 Effects of mesh size

To ensure that the results of the investigation into the geometric scaling are independent of the discretization a mesh sensitivity study was carried out first.

For this purpose, a straight cantilever beam, as represented in Fig. 2, is chosen as a reference case. The free end of this cantilever beam is subjected to a displacement u and the reaction force F is recorded. The beam is l = 0.1 m long and has a solid circular cross-section with a radius of r = 1 mm, resulting in a slenderness-ratio $S = l/r = 100$. The material

Fig. 2 Schematic of a cantilever beam under load

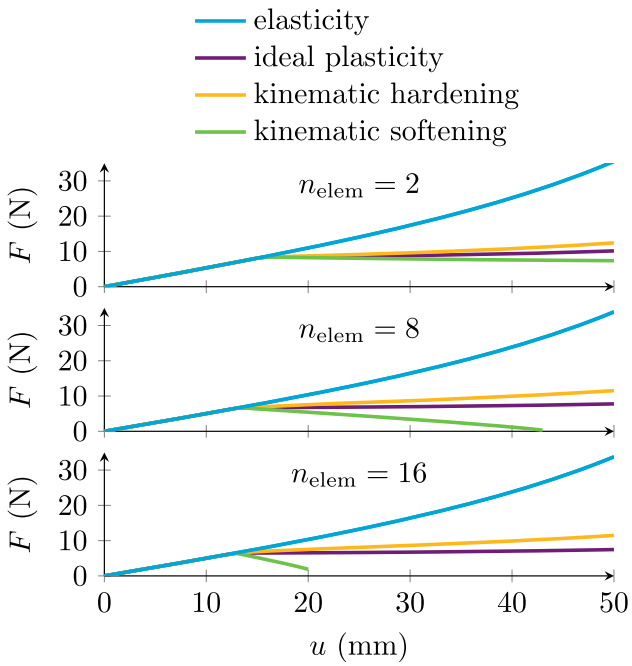

Fig. 3 Load displacement curves cantilever beam

has a Young's modulus of 210 GPa and a Poisson's ratio of 0.3.

All runs are investigated for elastic material behavior as well as ideal plastic and kinematic hardening plastic behavior. In order to gain insight into the effects of softening as well, runs are also conducted with the hardening tensor $\boldsymbol{H}$ given in Eq. 21 multiplied by -1. In this initial investigation a simplified yield surface with only yielding in the out of plane bending direction is used. This reduces Eq. 14 to:

$$\Phi = \left| \frac{M_1}{M_1^y - M_1^h} \right|^{\alpha_1^M} - 1 \leq 0. \tag{22}$$

Initially, simulations are done with $n_{\text{elem}} = 2, 8$ and 16 linear elements, respectively. The load displacement curves are depicted in Fig. 3. One can see a clear difference between the upper ($n_{\text{elem}} = 2$) and middle ($n_{\text{elem}} = 8$) discretizations depicted for all investigated material models. This difference disappears when comparing the middle and the lower graph, corresponding to $n_{\text{elem}} = 16$ elements. Following the onset of plasticity, the expected behavior can be observed in Fig. 3. In the case of ideal plasticity, a constant force is maintained after yielding. In contrast, models of hardening and softening

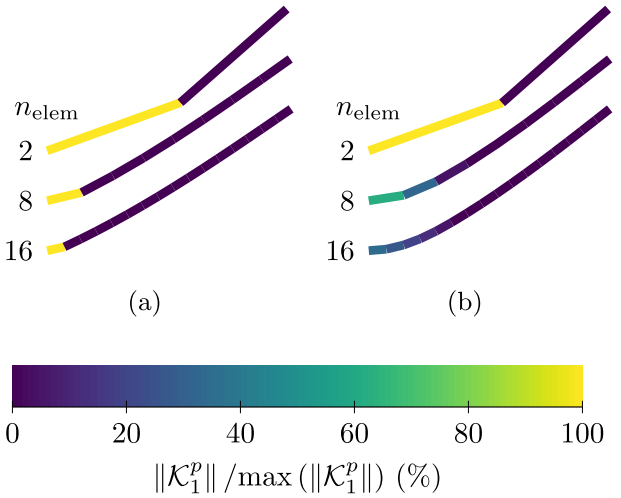

Fig. 4 Localization of plasticity for (a) ideal plasticity and (b) kinematic hardening plasticity ($n_{\text{elem}} = 2, 8$ and 16 from top to bottom; colors depict the relative distribution of plastic curvature)

plasticity exhibit a positive and negative slope, respectively, in the load displacement curve.

In Fig. 4a the distribution of the plastic curvature $\mathcal{K}_1^p$ is shown for a displacement of 50 mm using an ideally plastic material model. Again, in the figure, the three mesh refinements shown in the load–displacement curves are visualized, with $n_{\text{elem}} = 2, 8$ and 16 from top to bottom. It is clearly visible that plasticity is localized in one element at the clamped end of the beam. This stems from the fact, that the moment carried by the beam, due to the point load at the end, has its highest value at the left boundary. As soon as one element yields, this highest value is limited, thus limiting in turn the load the beam can bear. In the hardening case, the transmitted cross-sectional moment may increase due to hardening, leading to more subsequent elements starting to yield. This is visualized in Fig. 4b, where again the color corresponds to the plastic curvature $\mathcal{K}_1^p$ at a tip displacement of 50 mm. Again, the three refinements $n = 2, 8$ and 16 are shown from top to bottom. The softening case is not depicted due to the inability to achieve a converged solution at $u = 50$ mm.

To assess mesh sensitivity of the different material models, in Fig. 5 the forces for a deformation shortly after the onset of yielding at $u = 20$ mm in the upper graph and after a larger deformation at $u = 50$ mm in the lower graph are shown as function of the discretization of the beam. The comparison between the two graphs shows that the forces using ideal plasticity do not significantly change between the two displacement levels, which can be motivated by the fact, that as soon as a single element starts yielding, this element limits the effective load bearing capacity of the entire beam. In elasticity, however, the load bearing capacity is not limited and thus increases with increased displacement level. When introducing kinematic hardening into the formulation,

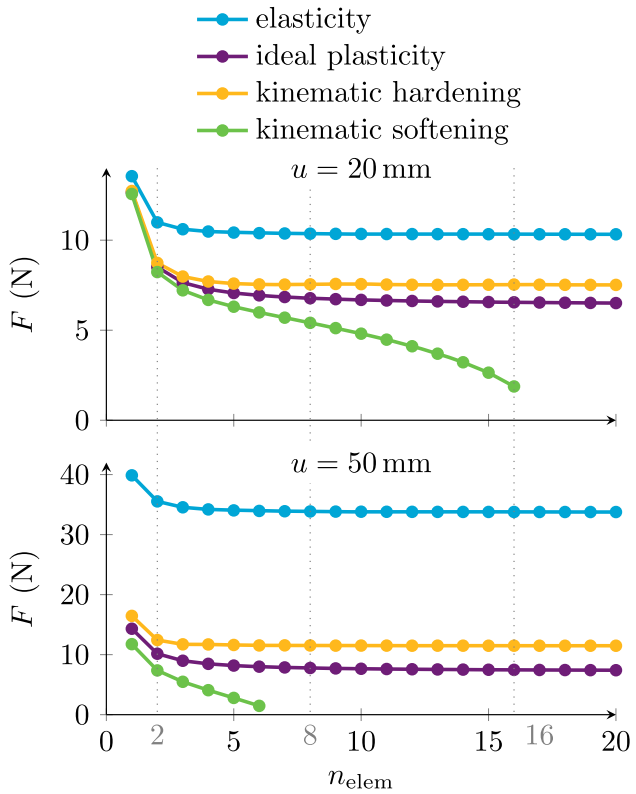

Fig. 5 Mesh convergence cantilever beam

one can clearly see, that the load limiting effect of yielding still persists, however less strong as in the ideal plastic case. Softening behavior, achieved by multiplying the hardening tensor $\boldsymbol{H}$ by -1, results in a clear mesh sensitivity as can be seen in the softening graphs in Fig. 5 at the two displacement levels. This mesh sensitivity problem is well-known and relates to the mathematical ill-posedness of the problem. Opposite to this, for the three cases of elasticity, ideal plasticity and kinematic hardening plasticity, one can observe mesh insensitivity for a large enough number of elements. For the investigated cantilever beam, eight elements are determined as sufficient to represent the global behavior of the system in these models. One should note, that this does not necessarily relate to the local phenomena, as seen in Fig. 4a, where a difference between the local distribution of plasticity for $n_{\text{elem}} = 8$ and $n_{\text{elem}} = 16$ can be observed around the left boundary. However, this has no effect on the global force response.

4 Effects of geometrical scaling

A key aspect of the design of lattice materials is the alteration of the length and orientation of the constituent beams, as well as the dimensions of the cross-section. As shown by [16] for circular and square cross-sections, the yield sur-

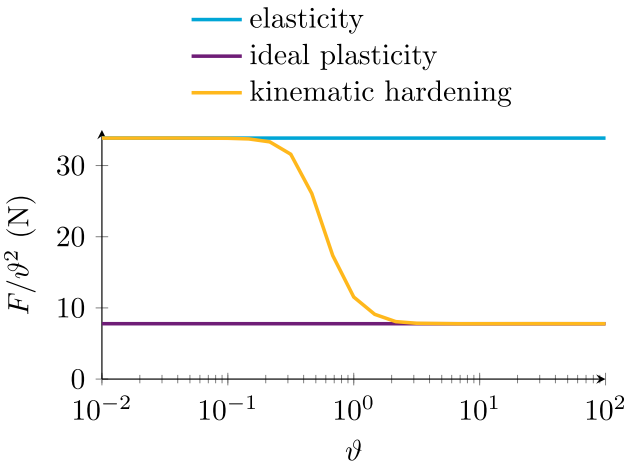

Fig. 6 Scaling study with an unscaled hardening tensor at $u = 50$ mm for the unscaled case

face is dependent on the scale of the geometric cross-section. [17] demonstrated the scaling of the hardening tensor with the microscale hardening parameter and its influence on the yield behavior of the beam for a circular cross-section. However, no attention has been given to the geometric scaling of this hardening tensor. In order to investigate this, the same cantilever beam as in Sect. 3 is investigated first. The material models for the beam are elasticity, ideal plasticity and kinematic hardening plasticity. Both geometric parameters, length and radius of the beam, are scaled uniformly with a scaling parameter $\vartheta \in [0.01, 100]$, resulting in the same slenderness ratio across the scales. The same simplified yield surface from the previous section as reported in Eq. 22 is employed and the *initial* yield stress resultant bending moment M_1^y is scaled with volume ϑ^3 since the elastic bending moment in a beam will scale likewise, as can be seen in the *implicit* scaling of the elastic stiffness tensor shown in Eq. 9.

4.1 Unscaled hardening tensor

In Fig. 6 the scaling behavior of the reaction force F/ϑ^2 is shown for the three investigated material models (elastic, ideal plastic and kinematic hardening) and the scaling parameter ϑ. The force is scaled back with ϑ^{-2}, since the force, similar to the moment, scales *implicitly* based on the elastic stiffness tensor from Eq. 9. For the elastic case as well for the ideal plastic case, no scale effect is observed. In the case of the kinematic hardening material model, however, a clear effect of the geometric scale is observed. For larger scaling factors $\vartheta > 1$ the behavior approaches the ideal plastic case, indicating a vanishing hardening effect, whereas for smaller scaling factors $\vartheta < 1$ the elastic case is approached, indicating an increase of the hardening effect relative to plasticity present in the model. In the following, we will investigate the cause for this spurious scale effect and propose a mitigation strategy.

4.2 Investigation into scaling effects

As previously demonstrated, the scale effect can be attributed to the kinematic hardening contribution. Therefore, the development of the hardening variables, denoted by $\boldsymbol{\mathcal{M}}$, as well as the hardening stresses, denoted by $\boldsymbol{\Sigma}^h$, is investigated. In order to investigate this, a single iteration of the return mapping scheme from Algorithm 1 in Sect. 2.2 is performed, initially for ideal plasticity and subsequently for hardening plasticity. Both the *implicit* scaling of the elastic properties and the yield surface are present throughout, with the scale variable, ϑ, *explicitly* given. To illustrate the scaling behavior at different stages of return mapping, we compute a single integration point with a bending moment of $M_1 = 0.6262\ \text{Nm}\vartheta^3$, just 1% above the yield limit of $M_1^y = 0.62\ \text{Nm}\vartheta^3$. For ideal plasticity the calculation is depicted in the first column of Table 1.

These results illustrate two characteristics of the underlying plasticity scheme. Firstly, plastic flow $\dot{\lambda}$ scales with area $\sim \vartheta^2$, which seems natural because in the present framework the stress resultant space is referred back to the rigid cross-section of the beam. Secondly, the presented return mapping scheme converges for the assumed simple yield surface in one iteration.

Next, we investigate the same problem with kinematic hardening. Here again, the elastic properties and the yield surface are scaled *implicitly*, without considering any scaling for the hardening tensor $\boldsymbol{H}$. The scale variable ϑ is again *explicitly* given. This is depicted in the second column of Table 1. Already at the end of **Step 3** it can be seen, that the update of plastic flow cannot be computed consistently with the *implicit, geometric* scaling in the stiffness tensor and no scaling in the hardening tensor. Comparing the results of the ideal plasticity term $\partial_{\boldsymbol{\Sigma}}\Phi \boldsymbol{C} \partial_{\boldsymbol{\Sigma}}\Phi = 1.915\vartheta^{-2}$ with the hardening plastic term $\partial_{\boldsymbol{\Sigma}^h}\Phi \boldsymbol{H} \partial_{\boldsymbol{\Sigma}^h}\Phi = 0.1779\vartheta^{-6}$ in the denominator of the computation of the plastic flow update (compare **Step 3** of Algorithm 1), we can now explain the behavior observed in Fig. 6. For small ϑ, hardening behavior dominates, leading to an almost elastic model, and for large ϑ, plastic behavior dominates, leading to an almost ideal plastic model.

4.3 Proposed mitigation strategy

To mitigate these spurious scale effects and ensure stable scaling in the computation of the plastic flow update, these two terms in the denominator will be further investigated. The *ideal plastic* term $\partial_{\boldsymbol{\Sigma}}\Phi \boldsymbol{C} \partial_{\boldsymbol{\Sigma}}\Phi$ scales with the area inverse $\sim \vartheta^{-2}$ due to the construction of the yield function and the *implicit* scaling of the stiffness matrix $\boldsymbol{C}$. The *harden-*

Table 1 Comparative iteration 0 and 1 through Algorithm 1 for the different material models

		Ideal plasticity	Hardening plasticity unscaled $\boldsymbol{H}$	scaled $\boldsymbol{H}$
Step 1	$\Delta\lambda^{(0)} =$	0	0	0
	$\mathcal{K}_1^{p\,(0)} =$	0	0	0
	$\mathcal{M}_1^{\mathcal{K}(0)} =$	–	0	0
	Iteration 0			
Step 2	$M_1 =$	$0.6262\vartheta^3$	$0.6262\vartheta^3$	$0.6262\vartheta^3$
	$M_1^h =$	–	$0\vartheta^0$	$0\vartheta^3$
	$\Phi^{(0)} =$	0.02101	0.02101	0.02101
Step 3	$\partial_{M_1}\Phi =$	$3.408\vartheta^{-3}$	$3.408\vartheta^{-3}$	$3.408\vartheta^{-3}$
	$\partial_{M_1^h}\Phi =$	–	$3.442\vartheta^{-3}$	$3.442\vartheta^{-3}$
	$\Delta^2\lambda =$	$0.01097\vartheta^2$	$\frac{0.02101}{1.915\vartheta^{-2}+0.1779\vartheta^{-6}}$	$0.01004\vartheta^2$
Step 4	$\Delta\lambda^{(1)} =$	$0.01097\vartheta^2$	$\lightning$	$0.01004\vartheta^2$
	$\mathcal{K}_1^{p\,(1)} =$	$0.03739\vartheta^{-1}$		$0.03421\vartheta^{-1}$
	$\mathcal{M}_1^{\mathcal{K}(1)} =$	–		$0.03455\vartheta^{-1}$
	Iteration 1			
Step 2	$M_1 =$	$0.62\vartheta^3$		$0.6206\vartheta^3$
	$M_1^h =$	–		$-0.0005188\vartheta^3$
	$\Phi^{(1)} =$	0.0001127		0.0001301

ing plastic term $\partial_{\boldsymbol{\Sigma}^h}\Phi\,\boldsymbol{H}\,\partial_{\boldsymbol{\Sigma}^h}\Phi$ on the other hand, needs to be adapted to obtain scaling with the area inverse and compute the same plastic flow for different geometric scales. As the partial derivative of the yield function is determined by the definition of the yield function, the only adaptable parameter is the hardening tensor $\boldsymbol{H}$. In the given case, it needs to be scaled similar to the material stiffness (for the bending moment $\sim \vartheta^4$) in order to achieve consistent geometrical scaling. With this, we can compute the return mapping again, as depicted in the last column of Table 1. Here, it becomes clear that the proposed approach to scale the hardening tensor leads to an elimination of the scaling inconsistencies and also to an algorithm that converges to the desired accuracy of $\Phi_{\text{tol}} = 1e-3$ within one iteration. This demonstrates, that the proposed strategy ensures the continuation of the return mapping scheme, without inconsistent scaling factors.

We will now examine the results of the proposed strategy for the response of the cantilever beam from Fig. 6. Figure 7 depicts the same loading cases, but with the hardening tensor scaled as explained earlier. The elastic and ideal plastic behavior is the same as reported in Fig. 6. The kinematic hardening plastic behavior shows the initially expected behavior, namely not exhibiting any scale effect. This demonstrates the applicability of the proposed strategy to mitigate scaling effects in hardening plasticity. This strategy will be explained in the next section for the generic yield function Eq. 14 together with an alternative strategy to scale the yield surface.

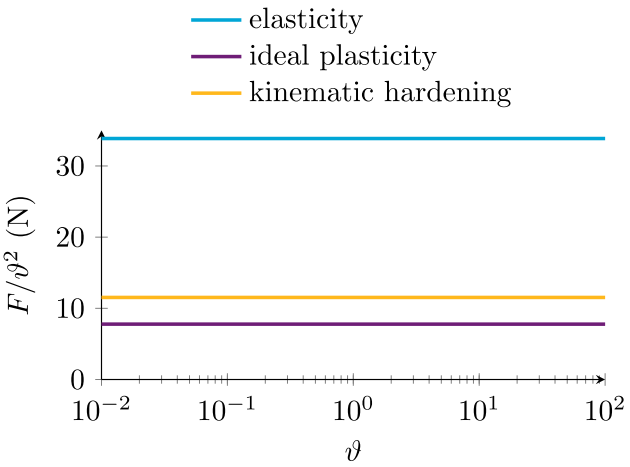

Fig. 7 Scaling study with a scaled hardening tensor (for the bending moment $\sim \vartheta^4$) at $u = 50\,mm$ for the unscaled case

5 Strategies for the consistent geometric scaling of hardening

When considering the yield function Eq. 14, we can derive the necessary scaling following the same approach. Initially, we assume again only the initial yield surface to be scaled. Investigation of the scaling of $\frac{\partial\Phi}{\partial\boldsymbol{\Sigma}^h}$ leads to the following:

$$\frac{\partial \Phi}{\partial \boldsymbol{\Sigma}^h} = \begin{bmatrix} (\dots)\,\frac{N_1}{(N_1^y - N_1^h)^2} \\ (\dots)\,\frac{N_2}{(N_2^y - N_2^h)^2} \\ (\dots)\,\frac{N_3}{(N_3^y - N_3^h)^2} \\ (\dots)\,\frac{M_1}{(M_1^y - M_1^h)^2} \\ (\dots)\,\frac{M_2}{(M_2^y - M_2^h)^2} \\ (\dots)\,\frac{M_3}{(M_3^y - M_3^h)^2} \end{bmatrix} \sim \begin{bmatrix} \vartheta^{-2} \\ \vartheta^{-2} \\ \vartheta^{-2} \\ \vartheta^{-3} \\ \vartheta^{-3} \\ \vartheta^{-3} \end{bmatrix}. \tag{23}$$

Taking this into account, we can derive, that the hardening tensor $\boldsymbol{H}$ needs to scale as

$$\boldsymbol{H}^\star = \begin{bmatrix} \boldsymbol{H}_{\varepsilon\varepsilon}\vartheta^2 & \boldsymbol{H}_{\varepsilon\kappa}\vartheta^3 \\ \boldsymbol{H}_{\kappa\varepsilon}\vartheta^3 & \boldsymbol{H}_{\kappa\kappa}\vartheta^4 \end{bmatrix}, \tag{24}$$

to ensure consistency of the plastic strains and internal hardening variables for different geometric scales. This scaling behavior is consistent with the *implicit* scaling of the elastic stiffness tensor $\boldsymbol{C}$ from Eq. 9. If, on the other hand, the scaling of the yield surface from [16] is interpreted not only for the *initial* yield surface but for the *entire* yield surface, the yield function from Eq. 14 becomes

$$\begin{aligned} \Phi = &\left|\frac{N_1}{(N_1^y - N_1^h)\vartheta^2}\right|^{\alpha_1^N} + \left|\frac{N_2}{(N_2^y - N_2^h)\vartheta^2}\right|^{\alpha_2^N} \\ &+ \left|\frac{N_3}{(N_3^y - N_3^h)\vartheta^2}\right|^{\alpha_3^N} + \left|\frac{M_1}{(M_1^y - M_1^h)\vartheta^3}\right|^{\alpha_1^M} \\ &+ \left|\frac{M_2}{(M_2^y - M_2^h)\vartheta^3}\right|^{\alpha_2^M} + \left|\frac{M_3}{(M_3^y - M_3^h)\vartheta^3}\right|^{\alpha_3^M} \\ &- 1 \\ &\leq 0, \end{aligned} \tag{25}$$

where the initial yield stress resultant forces and moments are *not* implicitly scaled and are taken as reported in Eq. 19. The derivative of the yield function with respect to the hardening stresses is then

$$\frac{\partial \Phi}{\partial \boldsymbol{\Sigma}^h} = \begin{bmatrix} (\dots)\,\frac{N_1}{(N_1^y - N_1^h)^2\vartheta^2} \\ (\dots)\,\frac{N_2}{(N_2^y - N_2^h)^2\vartheta^2} \\ (\dots)\,\frac{N_3}{(N_3^y - N_3^h)^2\vartheta^2} \\ (\dots)\,\frac{M_1}{(M_1^y - M_1^h)^2\vartheta^3} \\ (\dots)\,\frac{M_2}{(M_2^y - M_2^h)^2\vartheta^3} \\ (\dots)\,\frac{M_3}{(M_3^y - M_3^h)^2\vartheta^3} \end{bmatrix} \sim \begin{bmatrix} \vartheta^0 \\ \vartheta^0 \\ \vartheta^0 \\ \vartheta^0 \\ \vartheta^0 \\ \vartheta^0 \end{bmatrix}, \tag{26}$$

where we again need to keep in mind, that the current stress resultants are scaled *implicitly* via the scaling of the material stiffness tensor $\boldsymbol{C}$. In order to ensure, that the hardening term $\frac{\partial \Phi}{\partial \boldsymbol{\Sigma}^h}\boldsymbol{H}\frac{\partial \Phi}{\partial \boldsymbol{\Sigma}^h}$ scales with the area inverse ϑ^{-2}, the hardening tensor $\boldsymbol{H}$ needs to be scaled according to:

$$\boldsymbol{H}^\star = \boldsymbol{H}\vartheta^{-2}. \tag{27}$$

This strategy leads to identical results as scaling only the initial yield surface combined with the scaled hardening tensor in Eq. 24.

When using isotropic hardening of the form $\Phi = \dots + \Phi_y(1 + h_0)$, one can derive, that the hardening factor associated with the isotropic hardening variable needs to scale with the area inverse ϑ^{-2}, in the same manner.

Fig. 8 Schematic of a bent cantilever beam under load

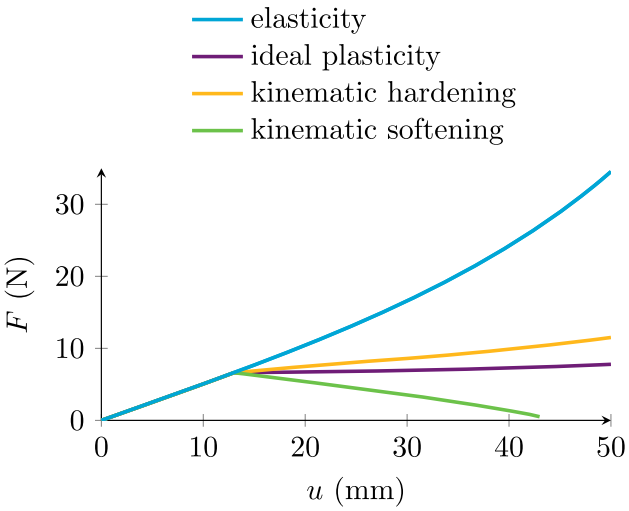

Fig. 9 Load displacement curves for the bent cantilever beam

5.1 Comparison of different hardening behavior in three dimensions

For an investigation in a fully three-dimensional setting, we use the same beam as previously, but it is now curved in a way, that the point of loading is angled 45°, resulting in a radius of ≈ 0.127 m. As illustrated in Fig. 8, the beam is loaded out of plane. Again, for all cases, 8 linear elements are used to describe the geometry. Load displacement curves for the material models, considered in Sect. 3, are shown in Fig. 9. To illustrate the scaling effect, different yielding

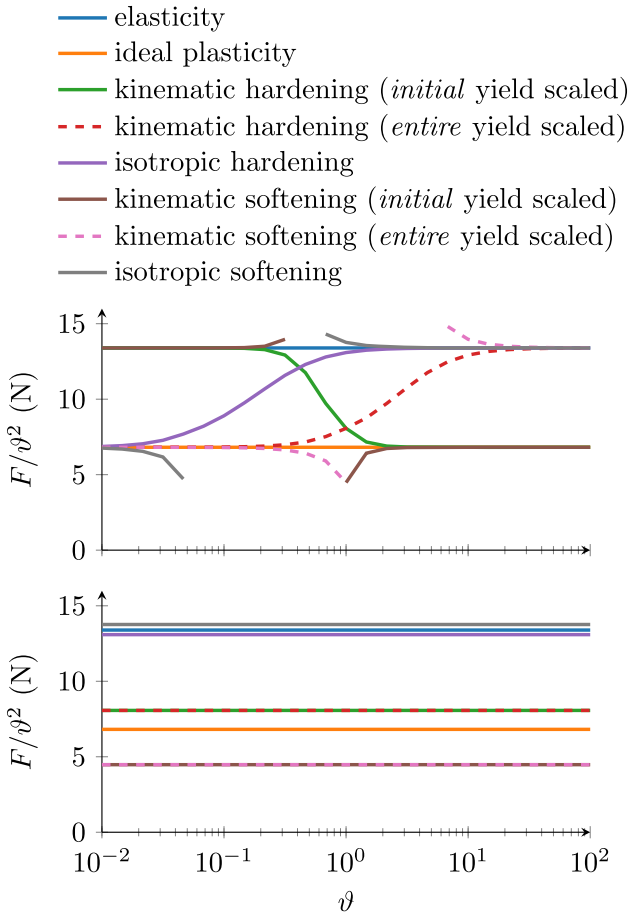

Fig. 10 Behavior of different yield functions, with the hardening tensor scaled (bottom), and with the hardening tensor unscaled (top) at $u = 25$ mm for the unscaled case

behavior (kinematic hardening and softening with scaling of the *initial* and scaling of the *entire* yield surface as well as isotropic hardening) is investigated. For the kinematic hardening cases, the values as given in Sect. 2.2 are used. For the scaling of the *initial* yield surface case, the yield function as given in Eq. 14 is employed, whereas in the case of scaling the *entire* yield surface, the modified surface as given in Eq. 25 is used. In the isotropic hardening case the same elastic properties are used. The yield function is constructed by taking Eq. 14 and adding the isotropic hardening term

$$\Phi_{\text{iso}} = \Phi - \zeta_H . \tag{28}$$

The hardening factor used in the corresponding calculations is set to be $H_{00} = 50$. The softening investigations are performed with the same values as the kinematic hardening investigations with the hardening tensor in Eq. 21 multiplied with -1. For isotropic softening, the hardening factor is set to $H_{00} = -50$. Initially, without the adaptation of the proposed scaling factors, clear scale effects are visible in the upper graph of Fig. 10 as well as non-physical behavior in the softening cases. The effect previously observed in Sect. 4.1, whereby the kinematic hardening model approaches the elastic case for ϑ and the ideal plastic case for large ϑ, is once again identified here for the model with the *initial* yield surface scaled. In contrast, the model with the *entire* yield surface scaled exhibits the opposite behavior, approaching the elastic case for large ϑ and the ideal plastic case for small ϑ. The non-physical effect, that softening computations show an even stiffer response at certain scaling factors compared to the purely elastic material is based in the fact, that the denominator in **Step 3** of Algorithm 1 can become negative if the second term with a negative $\boldsymbol{H}$ dominates the first term. This leads, under violation of the Karush-Kuhn-Tucker conditions in Eq. 18, to the non-physical effect of *negative* plastic flow. Therefore, plastic strains develop in the opposite direction of the total strain, which gives elastic strains being higher than total strains, and higher stresses than expected.

In consideration of the identified conditions, it is necessary to apply a scaling factor to the hardening tensor (or factor in the case of isotropic hardening) in accordance with the proposed mitigation strategy fitting to the yield surface. In the bottom graph of Fig. 10 it can be observed that the proposed strategy to modify the hardening tensor effectively eliminates the scale dependency of the behavior observed in all investigated cases. One has to note, that the chosen isotropic softening parameter is clearly non-physical as can be seen by the fact, that the response is stiffer than the purely elastic response.

5.2 Investigation of different slenderness ratios

Finally, we examine the behavior for different slenderness ratios $S = l/r$, with the length l and radius r of the beam. For this effect, we repeat the investigation from the previous section with two additional beams with different slenderness ratios $S = 10$ and 1000 as opposed to $S = 100$ as discussed above. For the slenderness ratio $S = 1000$, corresponding to a radius of $r = 0.1$ mm for $\vartheta = 1$, we do not observe any plasticity in the thin beams. This can be explained by the fact that all the material is relatively close to the neutral fiber of the beam and thus experiences less strain, leading to less plasticity effects when considering full cross-sections. Furthermore, by scaling only the cross-section, the stress resultant moments scale with ϑ^4, while the yield surface scales with ϑ^3. The curvature as a beam level strain prescriptor, corresponding to the stress-resultant bending moment, scales with ϑ^{-1}, requiring the scaling of the beam length as well as the boundary conditions with the geometry to maintain geometric similitude. On the other hand, the results for a beam with slenderness ratio $S = 10$, corresponding to $r = 10$ mm for $\vartheta = 1$, in Fig. 11, evidently show stronger plastic effects. While for the cross-section in Fig. 10 the relative reduction of the force required to enforce

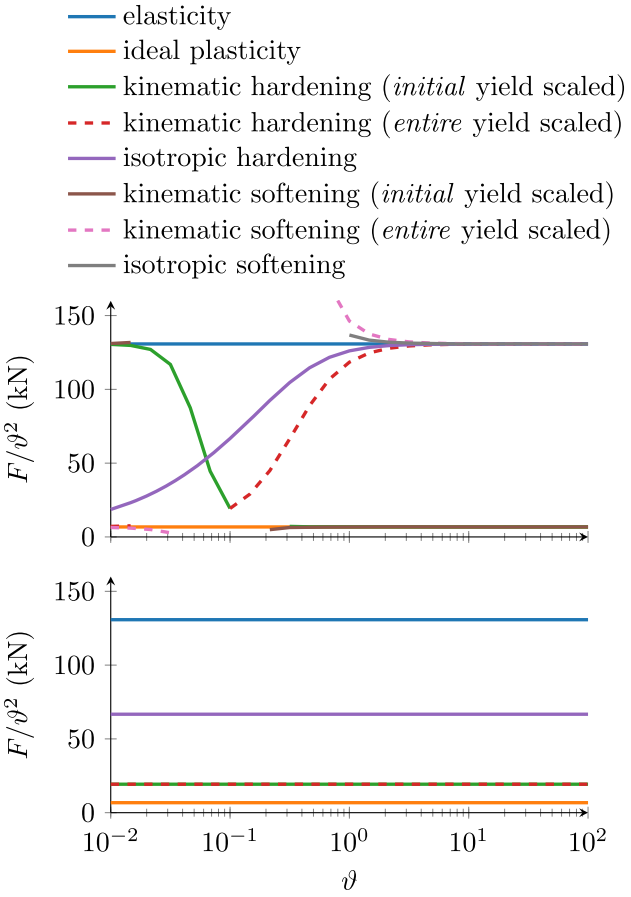

Fig. 11 Behavior of different yield functions, with the hardening tensor scaled (bottom), and with the hardening tensor unscaled (top) at $u = 25$ mm for the unscaled case ($S = 10$)

the deformation associated with ideal plasticity compared to elasticity is about a factor of 0.5, for the examined thicker beams this ratio is closer to 0.1. The stronger plastic effect can again be explained by the fact that the material is relatively further away from the neutral fiber and thus experiences more strain. This example again emphasizes the applicability of the proposed scaling strategy, as in the lower graph of Fig. 11 all size effects observed in the upper graph have been eliminated.

6 Conclusion

The incorporation of geometric scaling into the kinematic hardening of beams, has been demonstrated to successfully mitigate undesirable scale effects. We present a strategy for determining appropriate scaling of hardening parameters based on the yield function and its derivatives, and illustrate its applicability in a variety of scenarios with different yield functions as well as hardening or softening behavior. [16] have shown the issue of geometric scaling of the yield surface in ideal plasticity. This scaling can be interpreted in the kinematic hardening model derived by[17] in two ways: Either as *implicit* scaling of the *initial* yield surface by adapting the yield limits in the six directions depending on the size of the cross-section, or as *explicit* scaling of the *entire* yield surface. The proposed strategy is independent of the interpretation of the scaling of the yield surface, as it derives the scaling factors analytically from a given yield surface formulation. It is demonstrated that the undesirable scale effects can be mitigated and that the definition of a hardening tensor dependent on a specific geometric scale can be avoided. This approach will be particularly beneficial for the targeted architecture of nonlinear mechanical metamaterials undergoing large inelastic deformations. At large deformations, the influence of geometric properties on the nonlinear response of the structure is unknown and requires the fitting of model parameters for a large set of geometric scales. An easily adaptable plasticity formulation that incorporates the effects of geometric scale also in the hardening will circumvent the need for model calibration at a wide range of sizes. This framework enables the rapid design of architected nonlinear materials with lattice structures and their accurate representation at arbitrary scales.

Author Contributions **T. Gärtner:** Conceptualization, Data curation, Investigation, Methodology, Software, Validation, Visualization, Writing - original draft **S.J. van den Boom:** Conceptualization, Methodology, Supervision, Writing - review & editing **J. Weerheijm:** Funding acquisition, Writing - review & editing **L.J. Sluys:** Conceptualization, Funding acquisition, Methodology, Supervision, Writing - review & editing

Funding The project is financed by TNO through the PhD program of the Dutch Ministry of Defence.

Data availability Data will be made available upon request.

Declarations

Declaration of Conflict of interest The authors declare that they have no known competing financial interests or personal relationships that could have appeared to influence the work reported in this paper.

References

1. Saxena KK, Das R, Calius EP (2016) Three decades of auxetics research - materials with negative poisson's ratio: a review. Adv Eng Mater 18(11):1847–1870. https://doi.org/10.1002/adem.201600053
2. Crouch IG (2019) Body armour – new materials, new systems. Def Technol 15(3):241–253. https://doi.org/10.1016/j.dt.2019.02.002
3. Tahir D, Zhang M, Hu H (2022) Auxetic materials for personal protection: a review. Phys Statu Solidi (b) 259(12):2200324. https://doi.org/10.1002/pssb.202200324
4. Simo JC (1985) A finite strain beam formulation the three-dimensional dynamic problem part i. Compu Method Appl Mech Eng 49(1):55–70. https://doi.org/10.1016/0045-7825(85)90050-7
5. Reissner E (1981) On finite deformations of space-curved beams. ZAMP Zeitschrift für angewandte Mathematik und Physik 32(6):734–744. https://doi.org/10.1007/bf00946983
6. Antman SS (2005) Nonlinear problems of elasticity. Appl Math Sci. https://doi.org/10.1007/0-387-27649-1
7. Eugster SR (2015) Geometric continuum mechanics and induced beam theories. Lecture Notes Appl Compu Mech. https://doi.org/10.1007/978-3-319-16495-3
8. Tenorio-Montero E, Juárez-Luna G (2021) Beam-column finite element with embedded discontinuities for modelling damage in reinforced concrete prismatic elements. Structures 29:1934–1953. https://doi.org/10.1016/j.istruc.2020.12.055
9. Tojaga V, Gasser TC, Kulachenko A, Östlund S, Ibrahimbegovic A (2023) Geometrically exact beam theory with embedded strong discontinuities for the modeling of failure in structures part i: formulation and finite element implementation. Computer Methods Appl Mech Eng. https://doi.org/10.1016/j.cma.2023.116013
10. Smriti, Kumar A, Großmann A, Steinmann P (2018) A thermoelastoplastic theory for special cosserat rods. Mathe Mech Solids 24(3):686–700. https://doi.org/10.1177/1081286517754132
11. Smriti, Kumar A, Steinmann P (2020) A finite element formulation for a direct approach to elastoplasticity in special cosserat rods. Int J Numer Methods Eng. https://doi.org/10.1002/nme.6566
12. Weeger O, Valizadeh I, Mistry Y, Bhate D (2023) Inelastic finite deformation beam modeling, simulation, and validation of additively manufactured lattice structures. Add Manuf Lett. https://doi.org/10.1016/j.addlet.2022.100111
13. Karapiperis K, Radi K, Wang Z, Kochmann DM (2023) A variational beam model for failure of cellular and truss-based architected materials. Adv Eng Mater. https://doi.org/10.1002/adem.202300947
14. Simo JC, Hjelmstad KD, Taylor RL (1984) Numerical formulations of elasto-viscoplastic response of beams accounting for the effect of shear. Comput Methods Appl Mech Eng 42(3):301–330. https://doi.org/10.1016/0045-7825(84)90011-2
15. Duan L, Chen W-F (1990) A yield surface equation for doubly symmetrical sections. Eng Struct 12(2):114–119. https://doi.org/10.1016/0141-0296(90)90016-1
16. Herrnböck L, Kumar A, Steinmann P (2021) Geometrically exact elastoplastic rods: determination of yield surface in terms of stress resultants. Comput Mech 67(3):723–742. https://doi.org/10.1007/s00466-020-01957-4
17. Herrnböck L, Kumar A, Steinmann P (2022) Two-scale off-and online approaches to geometrically exact elastoplastic rods. Comput Mech 71(1):1–24. https://doi.org/10.1007/s00466-022-02204-8
18. Dynaflow Research Group: JIVE. https://dynaflow.com/software/jive/
19. Simo JC, Vu-Quoc L (1986) A three-dimensional finite-strain rod model part ii: computational aspects. Computer Methods Appl Mech Eng 58(1):79–116. https://doi.org/10.1016/0045-7825(86)90079-4
20. Crisfield MA, Jelenic G (1999) Objectivity of strain measures in the geometrically exact three-dimensional beam theory and its finite-element implementation. Procee Royal Soc Lond Ser A: Mathe, Phys Eng Sci 455(1983):1125–1147. https://doi.org/10.1098/rspa.1999.0352
21. Simo JC, Hughes TJR (1998) Computational inelasticity. Interdiscip Appl Math. https://doi.org/10.1007/b98904